

Conceptual Design of a Next-Generation All-Sky γ -ray Telescope Operating at TeV Energies

R.S. Miller ^{a,1}, S. Westerhoff ^b

^a*Neutron Science & Technology, Los Alamos National Laboratory, Los Alamos, NM 87545, USA*

^b*Santa Cruz Institute for Particle Physics, University of California, Santa Cruz, CA 95064, USA*

Abstract

The next generation all-sky monitor operating at TeV (0.1-30 TeV) energies should be capable of performing a continuous high sensitivity sky survey, and detecting transient sources, such as AGN flares, with high statistical significance on timescales of hours to days. We describe an instrument concept for a large area, wide aperture, TeV ground-based γ -ray telescope. The conceptual design is comprised of $\sim 20\,000$ $1\,\text{m}^2$ scintillator-based pixels arranged in a densely packed mosaic. In addition to fast timing, the dense array of pixels also provides a unique imaging capability; the shower image, the spatial distribution of secondary particles at ground level, can be exploited to identify and reject hadronic backgrounds. The good angular resolution and background rejection capabilities lead directly to high sensitivity, while retaining a large field of view, large effective area, and high duty cycle. An instrument such as the one described here complements the narrow field of view air-Cherenkov telescopes and could, in conjunction with future space-based instruments, extend the energy range for continuous monitoring of the γ -ray sky from MeV through TeV energies.

Key words: γ -ray telescopes; cosmic-ray detectors; extensive air showers

¹ corresponding author: richard@lanl.gov

1 Introduction

Very High Energy (VHE) γ -ray astronomy [1] is still in its infancy. Operating in the energy range from ~ 100 GeV to 30 TeV and beyond, this subfield of astronomy represents an exciting, relatively unsampled region of the electromagnetic spectrum, and a tremendous challenge. To develop more fully this field needs an instrument capable of performing continuous systematic sky surveys and detecting transient sources on short timescales without a priori knowledge of their location. These primary science goals require a telescope with a wide field of view and high duty cycle, excellent source location and background rejection capabilities - an instrument that complements both existing and future ground- and space-based γ -ray telescopes.

To be viable VHE astronomy must overcome a number of fundamental difficulties. Since the flux of VHE photons is small, telescopes with large collecting areas (10^3 m^2) are required to obtain statistically significant photon samples; telescopes of this size can, currently, only be located on the Earth's surface. However, VHE photons do not readily penetrate the ~ 28 radiation lengths of the Earth's atmosphere (1030 g/cm^2 thick at sea-level) but instead interact with air molecules to produce secondary particle cascades, or extensive air showers. Another difficulty of VHE astronomy is the large background of hadronic air showers, induced by cosmic-ray primaries (primarily protons), that cannot be vetoed.

In this paper we describe the conceptual design of an instrument that builds upon traditional extensive air shower methods; however, unlike typical extensive air shower arrays the detector design utilizes unique imaging capabilities and fast timing to identify (and reject) hadronic cosmic-ray backgrounds and achieve excellent angular resolution, both of which lead to improved sensitivity. In the following sections we briefly motivate the need for such an instrument (Section 2), discuss in detail telescope design parameters with emphasis on their optimization (Section 3), describe the conceptual design of a VHE telescope and the simulations used in this study (Section 4), and evaluate the capabilities of such a detector in terms of source sensitivity (Section 5). Finally, the results of this study are summarized and compared to both current and future VHE telescopes.

2 Motivation

VHE γ -ray astronomy has evolved dramatically in the last decade with the initial detections of steady and transient sources, galactic and extragalactic sources. To date 7 VHE γ -ray sources have been unambiguously detected [2–

8]; this contrasts dramatically with the number of sources detected in the more traditional regime of γ -ray astronomy at energies below ~ 20 GeV. The EGRET instrument aboard the Compton Gamma-Ray Observatory, for example, has detected pulsars, supernova remnants, gamma-ray bursts, active galactic nuclei (AGN), and approximately 50 unidentified sources in the 100 MeV-20 GeV range [9,10]. The power-law spectra of many EGRET sources show no sign of an energy cutoff, suggesting that they may be observable at VHE energies.

The 4 Galactic VHE objects, all supernova remnants, appear to have γ -ray emission that is constant in both intensity and spectrum. The 3 extragalactic VHE sources are AGN of the blazar class. Although AGN have been detected during both quiescent and flaring states, it is the latter that produce the most statistically significant detections. During these flaring states the VHE γ -ray flux has been observed to be as much as 10 times that of the Crab nebula - the standard candle of TeV astronomy [11].

Although observed seasonally since their initial detection, long term continuous monitoring of the TeV sources detected to date has never been possible, nor has there ever been a systematic survey of the VHE sky. This is primarily due to the fact that all VHE source detections to date have been obtained with air-Cherenkov telescopes. Because they are optical instruments, air-Cherenkov telescopes only operate on dark, clear, moonless nights - a $\sim 5 - 10\%$ duty cycle for observations; these telescopes also have relatively narrow fields of view ($\sim 10^{-2}$ sr). Although they are likely to remain unsurpassed in sensitivity for detailed source observations these telescopes have limited usefulness as transient monitors and would require over a century to complete a systematic sky survey.

The identification of additional VHE sources would contribute to our understanding of a range of unsolved astrophysical problems such as the origin of cosmic rays, the cosmological infrared background, and the nature of supermassive black holes. Unfortunately, the field of VHE astronomy is data starved; new instruments capable of providing continuous observations and all-sky monitoring with a sensitivity approaching that of the air-Cherenkov telescopes are therefore required. A VHE telescope with a wide field of view and high duty cycle could also serve as a high-energy early warning system, notifying space- and ground-based instruments of transient detections quickly for detailed multi-wavelength follow-up observations. Its operation should coincide with the launch of the next-generation space-based instrument such as GLAST [12].

Table 1

Figure of merit parameter definitions.

<i>Parameter</i>	<i>Units</i>	<i>Definition</i>
A_{eff}	m^2	(effective) detector area
T	sec	exposure
σ_θ	$^\circ$	angular resolution
R_γ	-	γ /hadron relative trigger efficiency
Q	-	γ /hadron identification efficiency

3 Figure of Merit Parameters

A conceptualized figure of merit is used to identify the relevant telescope design parameters. This figure of merit, also called the signal to noise ratio, can be written as

$$\left(\frac{signal}{noise}\right) \propto \frac{R_\gamma Q \sqrt{A_{eff} T}}{\sigma_\theta} \quad (1)$$

where the various parameters are defined in Table 1. Ultimately, source sensitivity is the combination of these design parameters. Although a more quantitative form of the figure of merit is used to estimate the performance of the conceptual telescope design (see Equation 5), we use Equation 1 to address specific design requirements.

3.1 R_γ

Air showers induced by primary particles in the 100 GeV to 10 TeV range reach their maximum particle² number typically at altitudes between 10 and 15 km above sea level (a.s.l.). An earth-bound detector therefore samples the cascade at a very late stage of its development, when the number of shower particles has already dropped by an order of magnitude from its value at shower maximum.

Figure 1 shows the result of computer simulations³ of the longitudinal profile of air showers induced in the Earth’s atmosphere by proton and γ -primaries

² Throughout the rest of the paper the generic term “particles” will refer to γ, e^\pm, μ^\pm , and hadrons unless otherwise noted.

³ Here and in the following analysis, the CORSIKA 5.61 [13] code is used for air-shower simulation in the atmosphere. It is briefly described in the next section.

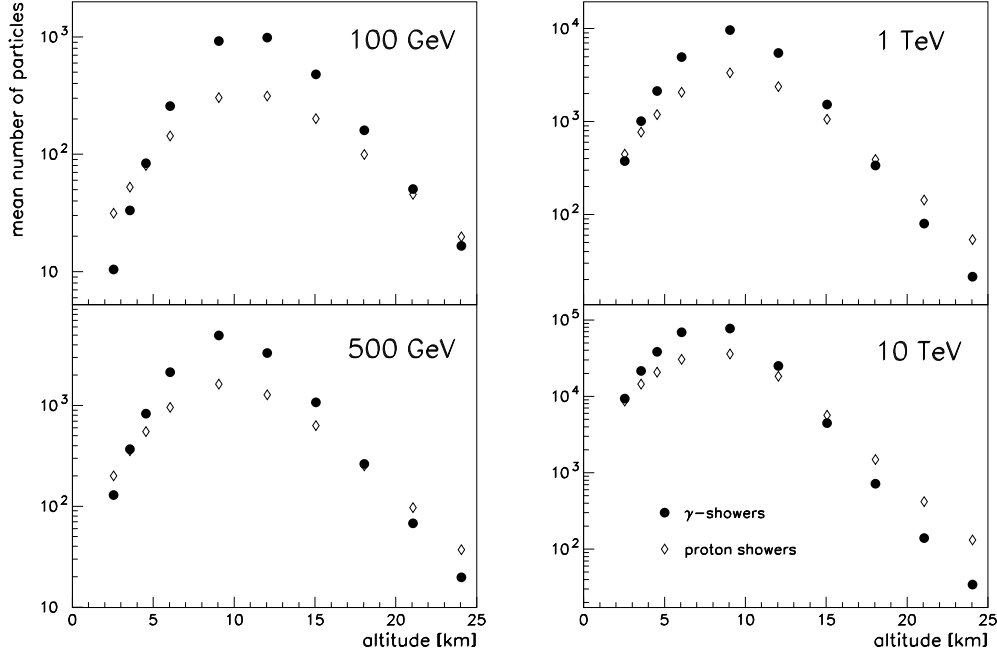


Fig. 1. Mean number of particles (γ, e^\pm, μ^\pm , hadrons) vs. altitude for proton- and γ -induced air showers with primary energies 100 GeV, 500 GeV, 1 TeV, and 10 TeV. The low energy cutoff of the particle kinetic energy is 100 keV (γ, e^\pm), 0.1 GeV (μ^\pm), and 0.3 GeV (hadrons).

with fixed energies and zenith angles $0^\circ \leq \theta \leq 45^\circ$. The small number of particles reaching 2500m detector altitude sets severe limits for observations at these altitudes. In addition, the number of particles in proton showers actually exceeds the number of particles in γ -showers at low altitudes (Figure 2). This implies that the trigger probability, and thus the effective area, of the detector is larger for proton than for γ -showers, an unfavorable situation which leads to an R_γ (the ratio of γ -ray to proton trigger efficiency) less than 1. At 4500 m, however, the mean number of particles exceeds the number at 2500 m by almost an order of magnitude at all energies. Therefore, telescope location at an altitude ≥ 4000 m is important for an air shower array operating at VHE energies not only because of the larger number of particles, and hence the lower energy threshold, but also because of the intrinsic γ /hadron-separation available, due to the relative trigger probabilities, that exists at higher altitudes.

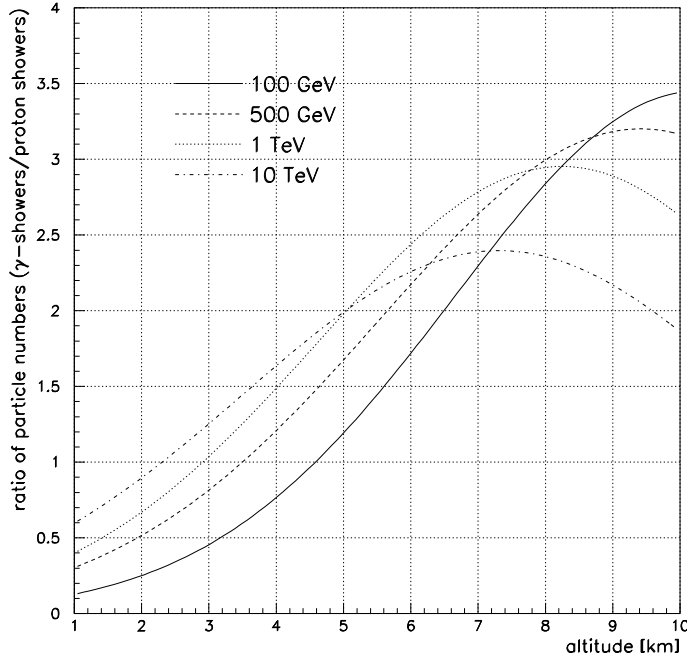


Fig. 2. Ratio of particle numbers in γ - and proton-induced showers vs. altitude.

3.2 Q

The rate of VHE γ -ray induced showers is significantly smaller than those produced by hadronic cosmic-rays⁴. Therefore rejecting this hadronic background and improving the signal to noise ratio is crucial to the success of any VHE γ -ray telescope. The effectiveness of a background rejection technique is typically expressed as a quality factor Q defined as

$$Q = \frac{\epsilon_\gamma}{\sqrt{1 - \epsilon_p}} \quad (2)$$

where ϵ_γ and ϵ_p are the efficiencies for *identifying* γ -induced and proton-induced showers, respectively. Traditional extensive air-shower experiments have addressed γ /hadron-separation (i.e. background rejection) by identifying the penetrating particle component of air showers (see e.g. [14,15]), particularly muons. Although valid at energies exceeding 50 TeV, the number of muons detectable by a telescope of realistic effective area is small at TeV energies (see Figure 3 (a)). In addition, the N_μ -distribution deviates from a Poisson distribution, implying that the fraction of proton showers *without* any muon is larger than $e^{-\bar{N}_\mu}$ (Figure 3 (b)). Relying on muon detection for an effective

⁴ At 1 TeV the ratio of proton- to γ -induced showers from the Crab Nebula is approximately 10^4 , assuming an angular resolution of 0.5 degrees.

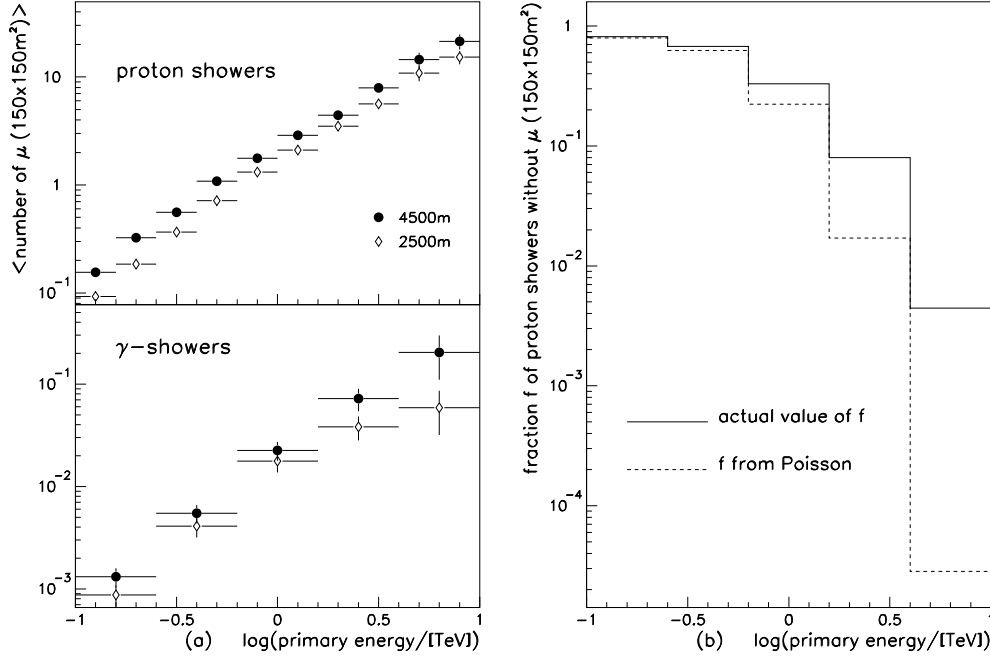


Fig. 3. For a $150 \times 150 \text{ m}^2$ detector area and cores randomly distributed over the detector area, (a) shows the mean number of μ^\pm in proton-induced showers as a function of the energy of the primary particle, and (b) shows the fraction f of proton showers without μ^\pm as a function of the energy of the primary particle. The solid line is the actual value of f , the dashed line is the expected value assuming the number of μ^\pm follows a Poisson distribution.

γ /hadron-separation requires efficient muon detection over a large area. A fine-grained absorption calorimeter to detect muons and perform air shower calorimetry can, in principle, lead to an effective rejection factor; however, the costs associated with such a detector are prohibitive.

In contrast to air-shower experiments, imaging air-Cherenkov telescopes have achieved quality factors $Q > 7$ by performing a *shape analysis* on the observed image [16]. Non-uniformity of hadronic images arises from the development of localized regions of high particle density generated by small sub-showers. Although some of the background rejection capability of air-Cherenkov telescopes is a result of their angular resolution, rejection of hadronic events by identifying the differences between γ - and proton-induced images considerably increases source sensitivity.

Although air-Cherenkov telescopes image the shower as it (primarily) appears at shower maximum, these differences should also be evident in the particle distributions reaching the ground. Figure 4 (top) shows the particle distributions reaching ground level for typical TeV γ -ray and proton-induced showers. This figure illustrates the key differences: the spatial distribution of particles

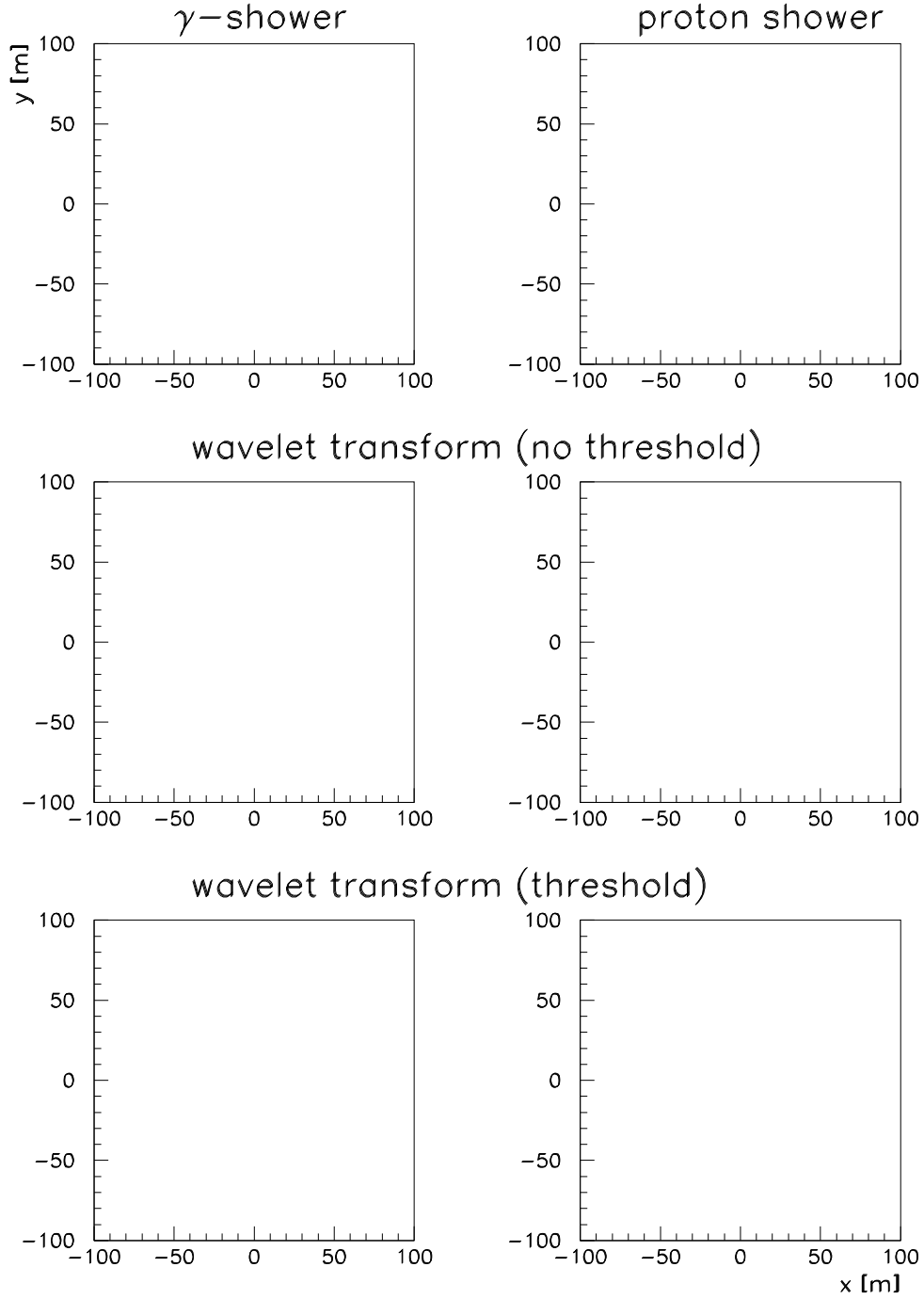


Fig. 4. Shower image (spatial particle distribution reaching ground level) for a typical TeV γ - and proton shower (top). Event image after convolution with “Urban Sombrero” smoothing function (middle), and after significance thresholding (bottom). (0,0) is the center of the detector.

in γ -ray showers tends to be compact and smooth, while in proton showers the distributions are clustered and uneven. Mapping the spatial distribution of shower particles (imaging), and identifying/quantifying shower features such as these should yield improved telescope sensitivity.

3.3 σ_θ

Shower particles reach the ground as a thin disk of diameter approximately 100 m. To first order, the disk can be approximated as a plane defined by the arrival times of the leading shower front particles. The initiating primary's direction is assumed to be a perpendicular to this plane. Ultimately, the accuracy with which the primary particle's direction can be determined is related to the accuracy and total number of the relative arrival time measurements of the shower particles,

$$\sigma_\theta \propto \frac{\sigma_t}{\sqrt{\rho}} , \quad (3)$$

where σ_t is the time resolution and ρ is the density of independent detector elements sampling the shower front. The telescope must, therefore, be composed of elements that have fast timing σ_t and a minimum of cross-talk since this can affect the shower front arrival time determinations. Once the detector area is larger than the typical lateral extent of air showers, thus providing an optimal lever arm, the angular resolution can be further improved by increasing the sampling density.

To achieve “shower limited” resolution, individual detector elements should have a time response no larger than the fluctuations inherent in shower particle arrival times (≤ 10 ns, see Figure 3 (c)); on the other hand, there is no gain if σ_t is significantly smaller than the shower front fluctuations.

In practice fitting the shower plane is complicated by the fact that the shower particles undergo multiple scattering as they propagate to the ground leading to a curvature of the shower front. This scattering delays the particle arrival time by $\mathcal{O}(\text{ns})/100$ m, however the actual magnitude of curvature is a function of the particle's distance from the core. Determination of the core position, and the subsequent application of a *curvature correction* considerably improves the angular resolution by returning the lateral particle distribution to a plane which can then be reconstructed. Core location accuracy can be improved by increasing the sampling density of detector elements and the overall size of the detector itself.

4 Conceptual Design

To summarize the previous sections, an all-sky VHE telescope should satisfy the following design considerations:

- $\sim 100\%$ duty cycle (T)
- large effective area (A_{eff})
- high altitude (> 4000 m)
- high sampling density
- fast timing
- imaging capability

In the sections that follow, we study how a pixellated *scintillator-based* large-area detector with 100% active sampling performs as an all-sky monitor and survey instrument. Scintillator is used since it can provide excellent time resolution and has high sensitivity to charged particles, ultimately leading to improvements in angular resolution, energy threshold, and background rejection. To reduce detector cross-talk, improve timing, and enhance the imaging capabilities the detector should be segmented into optically isolated pixels. This type of detector is easier to construct, operate, and maintain compared to other large-area instruments such as water- or gas-based telescopes - advantageous since the high altitude constraint is likely to limit potential telescope sites to remote locations.

Many of the design goals are most effectively achieved by maximizing the number of detected air-shower particles. As discussed in Section 3.1, detector altitude is of primary importance; however, at the energies of interest here only about 10% (Figure 5(a,b)) of the particles reaching the detector level are charged. Thus, the number of detected particles can be increased dramatically by improving the sensitivity to the γ -ray component of showers. A converter material (e.g. lead) on top of the scintillator converts photons into charged particles via Compton scattering and pair production, and, in addition, reduces the time spread of the shower front by filtering low energy particles which tend to trail the prompt shower front (Figure 5(c)) and thus deteriorate the angular resolution. Figure 5(d) shows the charged particle gain expected as a function of the converter thickness for lead, tin, and iron converters. The maximum gain is for a lead converter at ~ 2 radiation lengths ($1 \text{ r.l.} = 0.56 \text{ cm}$), but the gain function is rather steep below 1 r.l. and flattens above. Because of the spectrum of secondary γ -rays reaching the detector pair production is the most dominant process contributing to the charged particle gain (Figure 5(d)).

Techniques for reading out the light produced in scintillator-based detector elements have progressed in recent years with the development of large-area

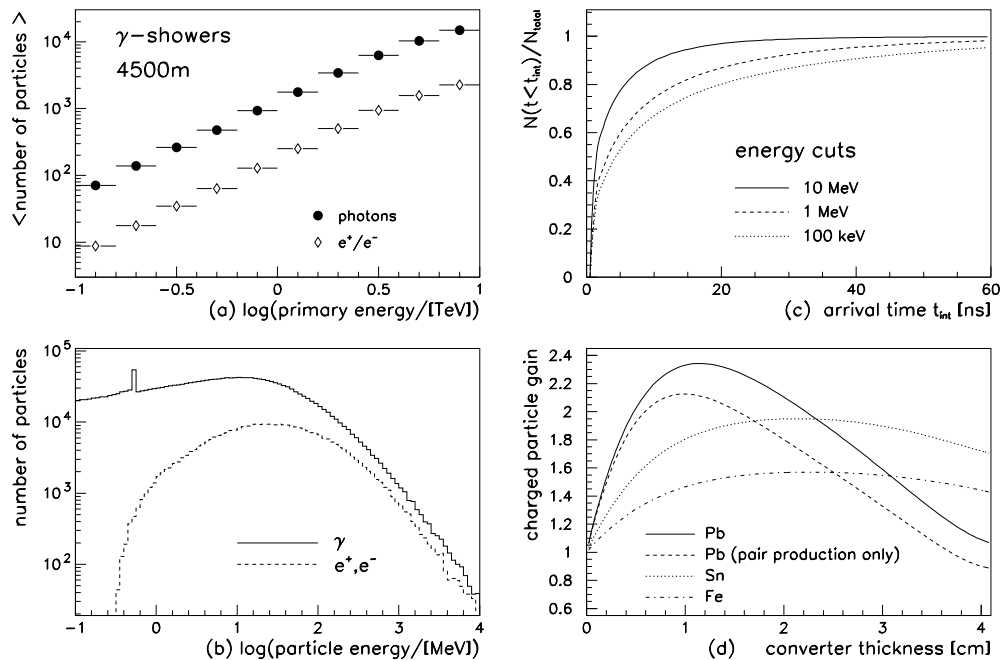


Fig. 5. Mean number vs. primary energy (a) and energy distribution (b) of secondary γ 's and e^\pm reaching 4500 m observation altitude. (c) Integral shower particle arrival time distribution for particles within 40 m distance to the core and various cuts on the particle energy (100 keV, 1 MeV, 10 MeV). (d) Charged particle gain as a function of the converter thickness for lead, tin, and iron converters.

sampling calorimeters. Of particular interest is the work by the CDF collaboration on scintillating tiles [17]; this technique utilizes fibers, doped with a wavelength shifter and embedded directly in the scintillator, to absorb the scintillation light and subsequently re-emit it at a longer wavelength. This re-emitted light is then coupled to photomultiplier tubes either directly or using a separate clear fiber-optic light guide. This highly efficient configuration is ideal for detecting minimum ionizing particles (MIPs), and produces 4 photoelectrons/MIP on average in a 5 mm-thick scintillator tile.

Using an array of tile/fiber detector elements one can now consider a large-area detector that counts particles and is $\sim 100\%$ active, and it is this paradigm that we discuss in more detail in the following sections. It should be noted that a scintillator-based air-shower detector is not a new idea; however, the use of the efficient tile/fiber configuration in a detector whose physical area is fully active pushes the traditional concept of an air-shower array to the extreme.

Table 2

Basic parameters of the shower and detector simulation.

zenith angle range	$0^\circ \leq \theta \leq 45^\circ$
lower kinetic energy cuts	0.1 MeV (e^\pm, γ) 0.1 GeV (μ^\pm) 0.3 GeV (hadrons)
scintillator thickness	0.5 cm
lead converter thickness	0.5 cm
PMT transit time spread	1 ns (FWHM)
average light yield/MIP	4 photoelectrons

4.1 Air Shower and Detector Simulation

The backbone of a conceptual design study is the simulation code. Here the complete simulation of the detector response to air showers is done in two steps: 1) initial interaction of the primary particle (both γ -ray and proton primaries) with the atmosphere and the subsequent development of the air shower, and 2) detector response to air-shower particles reaching the detector level.

The CORSIKA [13] air shower simulation code, developed by the KASCADE [18] group, provides a sophisticated simulation of the shower development in the Earth’s atmosphere. In CORSIKA, electromagnetic interactions are simulated using the EGS 4 [19] code. For hadronic interactions, several options are available. A detailed study of the hadronic part and comparisons to existing data has been carried out by the CORSIKA group and is documented in [13]. For the simulations discussed here, we use the VENUS [20] code for high energy hadronic interactions and GHEISHA [21] to treat low energy (≤ 80 GeV) hadronic interactions.

The simulation of the detector itself is based on the GEANT [22] package. The light yield of 0.5 cm tile/fiber assemblies has been studied in detail in [17] and [23], and we adopt an average light yield of 4 photoelectrons per minimum ionizing particle. This includes attenuation losses in the optical fibers and the efficiency of the photomultiplier. Simulation parameters are summarized in Table 2. It should be noted that wavelength dependencies of the fiber attenuation length and of the photomultiplier quantum efficiency have not been included.

As shown in Section 3.1 only a detector at an altitude above 4000 m can be expected to give the desired performance; however, we study the effect of

three detector altitudes, 2500 m (764.3 g cm^{-2}), 3500 m (673.3 g cm^{-2}), and 4500 m (591.0 g cm^{-2}), for the purpose of completeness. These altitudes span the range of both existing and planned all-sky VHE telescopes such as the Milagro detector [24] near Los Alamos, New Mexico (2630 m a.s.l.), and the ARGO-YBJ [25] detector proposed for the Yanbajing Cosmic Ray Laboratory in Tibet (4300 m a.s.l.).

5 Detector Performance

In the remainder of this paper we study the expected performance of a detector based on the conceptual design discussed above. Although the canonical design is a detector with a geometric area $150 \times 150 \text{ m}^2$, a detector design incorporating a $200 \times 200 \text{ m}^2$ area has also been analyzed in order to understand how telescope performance scales with area. Pixellation is achieved by covering the physical area of the detector with a mosaic of 5 mm thick scintillator tiles each covering an area of $1 \times 1 \text{ m}^2$.

5.1 Energy Threshold

The energy threshold of air-shower detectors is not well-defined. The trigger probability for a shower induced by a primary of fixed energy is not a step-function but instead rises rather slowly due to fluctuations in the first interaction height, shower development, core positions, and incident angles. Figure 6 (a) shows the trigger probability as a function of the primary γ -ray energy for three trigger conditions.

Typically, the primary energy where the trigger probability reaches either 10 % or 50 % is defined as the energy threshold (see Figure 6 (a)). A large fraction of air showers that fulfill the trigger condition will have lower energies since VHE source spectra appear to be power-laws, $E^{-\alpha}$. A more meaningful indication of energy threshold then is the *median* energy E_{med} ; however, this measure depends on the spectral index of the source. For a source with spectral index $\alpha = 2.49$ (Crab), Figure 6 (b, top) shows E_{med} as a function of detector altitude (for fixed detector size). The median energy increases as altitude decreases since the number of particles reaching the detector level is reduced at lower altitudes. For a detector at 4500 m a.s.l., E_{med} is about 500 GeV after imposing a 40 pixel trigger criterion.

E_{med} is not a strong function of the detector size (Figure 6 (b, bottom)). It is also noteworthy that a larger pixel size of $2 \times 2 \text{ m}^2$ instead of $1 \times 1 \text{ m}^2$ only slightly increases E_{med} ; due to the lateral extent of air showers and the large

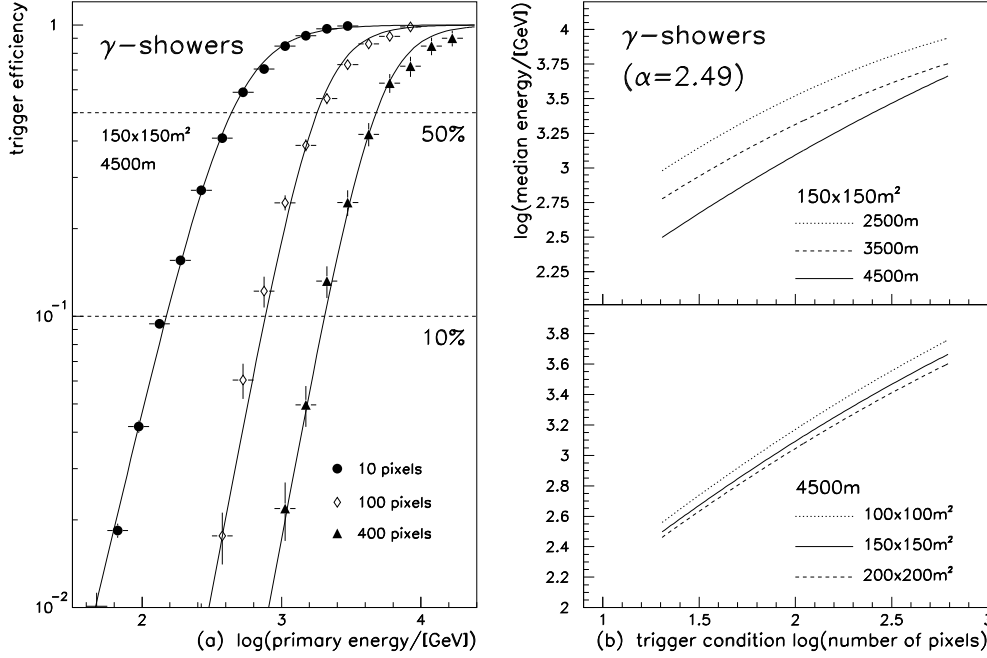


Fig. 6. (a) Trigger efficiency as a function of the primary particles' energy for three trigger conditions (10, 40, 400 pixels). (b) Median energy of detected γ -showers as a function of the trigger condition (number of pixels) for three detector altitudes (top) and as a function of the detector size for a fixed altitude (4500 m) (bottom).

average distances between particles, nearly 95 % of all showers with more than 50 m^2 -pixels also have more than 50 m^2 -pixels.

5.2 Background Rejection and Core Location

Due to its pixellation and 100% active area the telescope described here can provide true images of the spatial distribution of secondary particles reaching the detector. Image analysis can take many forms; the method of wavelet transforms [26] is well suited for identifying and extracting localized image features. To identify localized high-density regions of particles an image analysis technique that utilizes digital filters is used; the procedure is briefly summarized below while details are given in [27].

Proton- and γ -induced showers can be identified by counting the number of “hot spots”, or peaks, in a shower image in an automated, unbiased way. These peaks are due to small sub-showers created by secondary particles and are more prevalent in hadronic showers than in γ -induced showers. To begin, the shower image (i. e. the spatial distribution of detected secondary particles) is convolved with a function that smooths the image over a predefined region

or length scale (see Figure 4 (middle)). The smoothing function used in this analysis is the so-called “Urban Sombrero”⁵ function:

$$g\left(\frac{r}{a}\right) = \left(2 - \frac{r^2}{a^2}\right) e^{-\frac{r^2}{2a^2}} \quad (4)$$

where r is the radial distance between the origin of the region being smoothed and an image pixel, and a is the length scale over which the image is to be smoothed. This function is well suited for this analysis since it is a localized function having zero mean; therefore, image features analyzed at multiple scales a will maintain their location in image space. A peak’s maximum amplitude is found on length scale a corresponding to the actual spatial extent of the “hot spot.”

Many peaks exist in these images; the key is to tag statistically significant peaks. To do this the probability distribution of peak amplitudes must be derived from a random distribution of pixels. Using 2×10^4 events, each with a random spatial particle distribution, the probability of observing a given amplitude is computed. This is done for events with different pixel multiplicities and for different scale sizes. Results using only a single scale size of 8 m are presented here. This scale size represents the optimum for the ensemble of showers; scale size dependence as a function of pixel multiplicity is studied in [27]. In order to identify statistically significant peaks a threshold is applied to the smoothed image. Peaks are eliminated if the amplitude was more probable than 6.3×10^{-5} corresponding to a significance of $< 4\sigma$; the value of the threshold is chosen to maximize the background rejection. Figure 4 (bottom) shows the result of thresholding. After applying thresholding the number of significant peaks is counted; if the number of peaks exceeds the mean number of peaks expected from γ -induced showers then the event is tagged as a “proton-like” shower and rejected. The number of expected peaks is energy dependent starting at 1 peak (i. e. the shower core), on average, for γ -showers with less than 100 pixels and increasing with pixel multiplicity; proton-induced showers show a similar behavior except that the number of peaks rises faster with the number of pixels (see Figure 7).

Additional background rejection may be possible by using information such as the spatial distribution of peaks and the actual shape of individual peak regions. This is currently being investigated. The ability to map and analyze the spatial distributions of air shower particles implies that, in conjunction with analysis techniques such as the one described here, the large cosmic-ray induced backgrounds can be suppressed thereby improving the sensitivity of a ground-based air-shower array; quantitative results on the use of this image analysis technique are described below and summarized in Figure 10.

⁵ Also known as the “Mexican Hat” function.

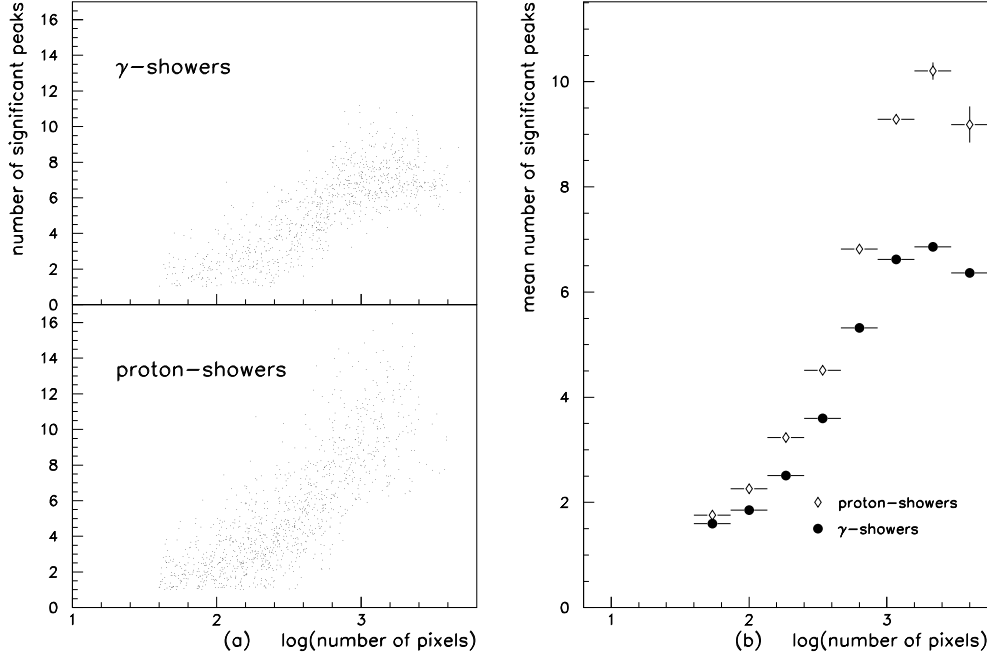


Fig. 7. (a) Number of significant peaks for γ - (top) and proton showers (bottom) as a function of pixel multiplicity. A random probability of $< 6.3 \times 10^{-5}$ is used to define a significant peak. (b) Mean number of significant peaks for γ - and proton showers as a function of pixel multiplicity.

Image analysis can also be used to identify and locate the shower core. Here the core is identified as the peak with the largest amplitude; this is reasonable assuming that typically the core represents a relatively large region of high particle density. Figure 8 (a) shows the accuracy of the core fit; other methods are less accurate and more susceptible to detector edge effects and local particle density fluctuations.

The core location is used to correct for the curvature of the shower front and to veto events with cores outside the active detector area. Rejecting “external” events is beneficial as both angular resolution and background rejection capability are worse for events with cores off the detector. We define the outer 10 m of the detector as a veto ring and restrict the analysis to events with fitted cores inside the remaining fiducial area ($130 \times 130 \text{ m}^2$ or $180 \times 180 \text{ m}^2$ for the $200 \times 200 \text{ m}^2$ design). This cut identifies and keeps 94 % of the γ -showers with *true* cores within the fiducial area while vetoing 64 % of events with cores outside. It is important to note that the non-vetoed events are generally of higher quality (better angular resolution, improved γ /hadron-separation). In addition, R_γ is smaller for external events than for internal ones due to the larger lateral spread of particles in proton showers; thus the veto cut actually improves overall sensitivity even though total effective area is decreased.

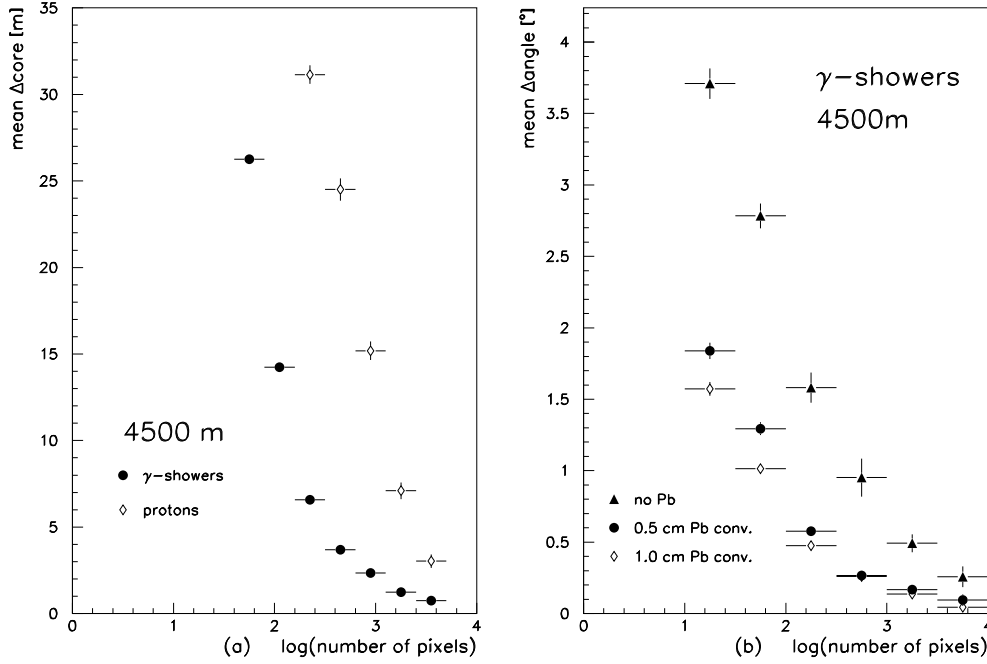


Fig. 8. (a) Mean distance between reconstructed and true shower core location. (b) Mean angle between reconstructed and true shower direction for a detector without lead converter and with 0.5 cm and 1.0 cm lead.

5.3 Angular Resolution

The shower direction is reconstructed using an iterative procedure that fits a plane to the arrival times of the pixels and minimizes χ^2 . Before fitting, the reconstructed core position (see Section 5.2) is used to apply a curvature correction to the shower front. In the fit, the pixels are weighted with $w(p) = 1/\sigma^2(p)$, where $\sigma^2(p)$ is the RMS of the time residuals $t_{pixel} - t_{fit}$ for pixels with p photoelectrons. t_{fit} is the expected time according to the previous iteration.

In order to minimize the effect of large time fluctuations in the shower particle arrival times, we reject pixels with times t_{pixel} with $|t_{pixel} - t_{fit}| \geq 10$ ns. In addition, only pixels within 80 m distance to the shower core are included in the fit.

Figure 8 (b) shows the mean difference between the fitted and the true shower direction as a function of the number of pixels for a detector with and without 0.5 cm and 1.0 cm of lead, again indicating the benefits of the converter. The angular resolution does not improve considerably when the converter thickness is increased from 0.5 cm to 1.0 cm, thus 0.5 cm is a reasonable compromise considering the tradeoff between cost and performance.

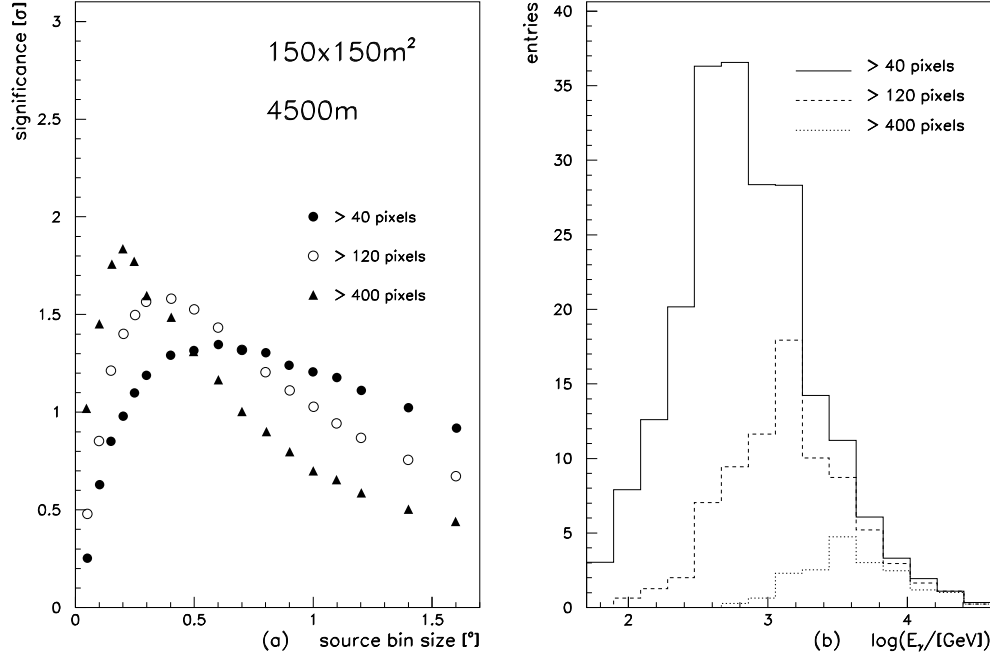


Fig. 9. (a) Significance for a one day observation of a Crab-like source for three trigger conditions (40, 120, 400 pixels) as a function of the source bin size. (b) Energy distribution of the detected γ -showers for the three trigger conditions. The source location is $|\delta - \lambda| \simeq 5^\circ$, where δ is the source declination and λ is the latitude of the detector site.

5.4 Sensitivity

The ultimate characteristic of a detector is its sensitivity to a known standard candle. In this section, the methods described so far are combined to estimate the overall point source sensitivity of a pixellated scintillation detector. As indicated in Equation 1, the sensitivity of an air shower array depends on its angular resolution σ_θ , its effective area A_{eff} , the trigger probabilities for source and background showers, and the quality factor of the γ /hadron-separation. However, as most of the parameters are functions of the primary energy, the sensitivity depends on the spectrum of the cosmic ray background and the spectrum of the source itself. The significance S therefore has to be calculated using

$$S = \frac{\int A_\gamma^{eff}(E) \epsilon_\gamma(E) J_\gamma(E) dE f_\gamma T}{\sqrt{\int A_p^{eff}(E) (1 - \epsilon_p(E)) J_p(E) dE \Delta\Omega T}} \quad (5)$$

where J_γ and J_p are the photon and proton energy spectrum, and f_γ is the fraction of γ -showers fitted within the solid angle bin $\Delta\Omega = 2\pi(1 - \cos\theta)$.

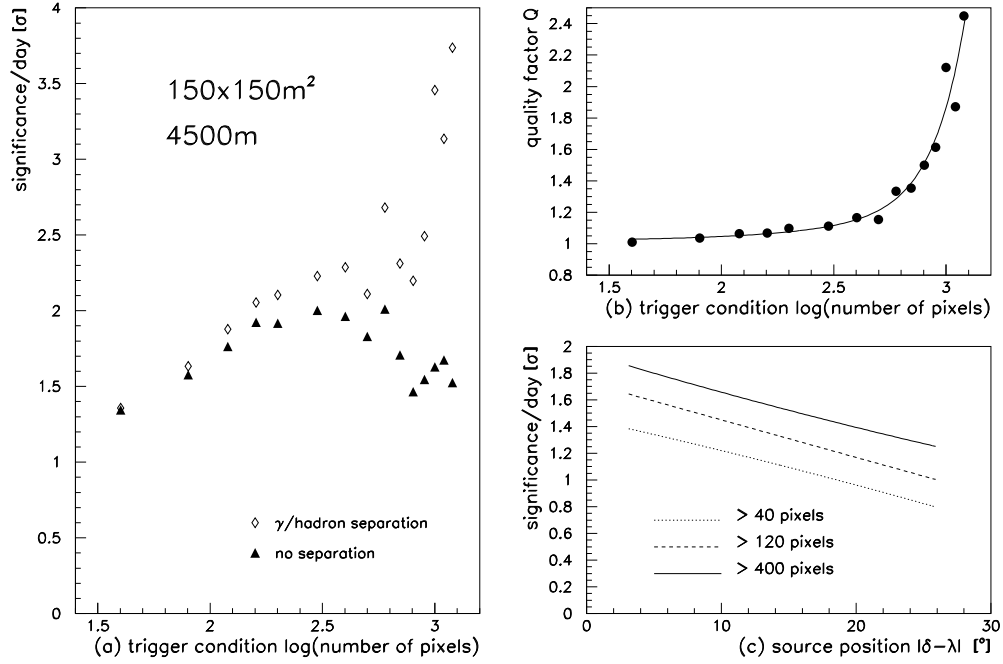


Fig. 10. (a) Significance/day for a Crab-like source as a function of the trigger condition with and without γ /hadron-separation for the $150 \times 150 \text{ m}^2$ prototype. (b) Quality factor as a function of the trigger condition. (c) Sensitivity as a function of the source position $|\delta - \lambda|$.

Other parameters have their standard meaning.

The Crab Nebula is commonly treated as a standard candle in γ -ray astronomy; this allows the sensitivity of different telescopes to be compared. The differential spectrum of the Crab at TeV energies has been measured by the Whipple collaboration [28]:

$$J_\gamma(E) = (3.20 \pm 0.17 \pm 0.6) \times 10^{-7} E_{\text{TeV}}^{-2.49 \pm 0.06 \pm 0.04} \text{ m}^{-2} \text{ s}^{-1} \text{ TeV}^{-1}. \quad (6)$$

The sensitivity of the detector to a Crab-like source can be estimated using Equation 5 and the differential proton background flux measured by the JACEE balloon experiment [29]:

$$\frac{dJ_p(E)}{d\Omega} = (1.11^{+0.08}_{-0.06}) \times 10^{-1} E_{\text{TeV}}^{-2.80 \pm 0.04} \text{ m}^{-2} \text{ sr}^{-1} \text{ s}^{-1} \text{ TeV}^{-1}. \quad (7)$$

Calculating S using Equation 5 is not straightforward since ϵ_γ is not a constant, but rather a function of the event size and core position and, therefore, angular reconstruction accuracy. This equation can be solved, however, by a Monte Carlo approach: Using the Crab and cosmic-ray proton spectral indices, a

pool of simulated γ - and proton showers ($\mathcal{O}(10^6)$ events of each particle type at each altitude) is generated with energies from 50 GeV to 30 TeV and with zenith angles $0^\circ \geq \theta \geq 45^\circ$. A full Julian day source transit can be simulated for a given source bin size and declination by randomly choosing γ -ray and proton-induced showers from the simulated shower pools at rates given by Equations 6 and 7. The only constraint imposed on the events is that they have the same zenith angle as the source bin at the given time. The showers are then fully reconstructed, trigger and core location veto cuts, as well as γ /hadron-separation cuts, are applied; γ -showers are required to fall into the source bin. This procedure produces distributions of pixel multiplicity, core position, etc. reflecting instrumental resolutions and responses.

Because the angular resolution varies with the number of pixels, the optimal source bin size also varies. Figure 9 (a) shows the significance for a full-day observation of a Crab-like source with $|\delta - \lambda| \simeq 5^\circ$, where δ is the source declination and λ is the latitude of the detector site, as a function of the source bin size for three trigger conditions. As the number of pixels increases, the optimal source bin size decreases from 0.6° (40 pixels) to 0.2° (400 pixels). Figure 9 (b) shows how the energy distribution of detected γ -showers changes with trigger condition. The median energy for a 40 pixel trigger is 600 GeV, with a substantial fraction of showers having energies below 200 GeV. For a 120 pixel trigger, E_{med} is 1 TeV.

For a 1 day Crab-like source transit, Figure 10 (a) shows how the significance varies as a function of the trigger condition with and without γ /hadron-separation. If no γ /hadron-separation is applied the sensitivity increases and then falls above 500 pixels because of the finite size of the detector. However, as shown in Section 5.2, above 500 pixels the quality factor of the γ /hadron-separation counterbalances the loss of area. Figure 10 (b) shows the quality factor derived solely from the ratio of source significance with and without separation. As expected, Q increases dramatically with pixel number, leading to significances well above 3σ per day for energies above several TeV. The sensitivity also depends on the declination of the source. Results quoted so far refer to sources $|\delta - \lambda| \simeq 5^\circ$. Figure 10 (c) shows how the expected significance per source day transit changes with the source declination δ .

Table 3 summarizes the dependence of the detector performance on the size and the altitude of the detector. Significance scales with $\sqrt{A_{eff}}$ as expected from Equation 1. Detector altitude, however, is more critical. Although at 2500 m 10σ detections of a steady Crab-like source per year are possible, it is only at 4000 m altitudes where the sensitivity is sufficient to detect statistically significant daily variations of source emissions.

It is noteworthy that for the canonical design at 4500 m, a trigger condition as low as 10 pixels still produces 1.2σ per day at median energies of about

Table 3

Significances S for a 1 day observation of a Crab-like source with $|\delta - \lambda| \simeq 5^\circ$ for different altitudes and trigger conditions. E_{med} is the median energy of the detected source particles, values in parentheses denote significances after γ /hadron separation.

		$150 \times 150 \text{ m}^2$		$200 \times 200 \text{ m}^2$	
altitude	trigger	$S [\sigma]$	$\log(E_{med}^{\text{GeV}})$	$S [\sigma]$	$\log(E_{med}^{\text{GeV}})$
4500 m	40	1.3 (1.3)	2.8	1.8 (1.8)	2.8
	1000	1.6 (2.5)	3.8	1.9 (2.7)	3.8
3500 m	40	0.9 (0.9)	3.1	1.2 (1.2)	3.0
	1000	0.8 (1.2)	4.1	1.3 (1.7)	4.0
2500 m	40	0.4 (0.4)	3.3	0.6 (0.6)	3.2
	1000	0.5 (0.6)	4.3	0.8 (1.1)	4.2

Table 4

Expected rates [kHz] for a $150 \times 150 \text{ m}^2$ detector at different altitudes. Cores are randomly distributed over $300 \times 300 \text{ m}^2$ and no core veto cut is applied.

trigger	4500 m	3500 m	2500 m
10	34.5	18.9	10.5
40	6.7	3.6	2.1
100	1.8	1.0	0.6
400	0.2	0.2	0.1
1000	0.05	0.04	0.02

280 GeV corresponding to an event rate of 34.5 kHz. Predicted event rates for different trigger conditions at various altitudes are summarized in Table 4. Sustained event rates below $\sim 10 \text{ kHz}$ are achievable with off-the-shelf data acquisition electronics; higher rates may also be possible. The event rates estimated here are relatively low compared to the rate of single cosmic-ray muons; because of the optical isolation and low-cross talk of individual detector elements single muons are unlikely to trigger the detector even with a low pixel multiplicity trigger condition.

6 Conclusion

To fully develop the field of VHE γ -ray astronomy a new instrument is required - one capable of continuously monitoring the sky for VHE transient emission and performing a sensitive systematic survey for steady sources. To achieve these goals such an instrument must have a wide field of view, $\sim 100\%$ duty cycle, a low energy threshold, and background rejection capabilities. Combining these features we have shown that a detector composed of individual scintillator-based pixels and 100% active area provides high sensitivity at energies from 100 GeV to beyond 10 TeV. Detailed simulations indicate that a source with the intensity of the Crab Nebula would be observed with an energy dependent significance exceeding $\sim 3\sigma/\text{day}$. AGN flares, or other transient phenomena, could be detected on timescales $\ll 1$ day depending on their intensity - providing a true VHE transient all-sky monitor. A conservative estimate of the sensitivity of a detector like the one described here (the PIXIE telescope) is shown in Figure 11 compared to current and future ground- and space-based experiments. The plot shows the sensitivities for both 50 hour and 1 year source exposures, relevant for transient and quiescent sources, respectively. A detector based on the PIXIE design improves upon first-generation detector concepts, such as Milagro, in two principal ways: fast timing and spatial mapping of air shower particles. The sensitivity of a sky map produced by this detector in 1 year reaches the flux sensitivity of current air-Cherenkov telescopes (for a 50 hour exposure), making the detection of AGN in their quiescent states possible.

The cost for a detector based on the conceptual design outlined is estimated conservatively at between \$500 and \$1000 per pixel; the cost of scintillator is the dominant factor. A proposal to perform a detailed detector design study (evaluation of detector materials, data acquisition prototyping, and investigation of construction techniques) leading to a final design is currently pending.

Although unlikely to surpass the sensitivity of air-Cherenkov telescopes for detailed single source observations, a sensitive all-sky VHE telescope could continuously monitor the observable sky at VHE energies. In summary, non-optical ground-based VHE astronomy *is* viable, and the development of an all-sky VHE telescope with sensitivity approaching that of the existing narrow field of view air-Cherenkov telescopes, will contribute to the continuing evolution of VHE astronomy.

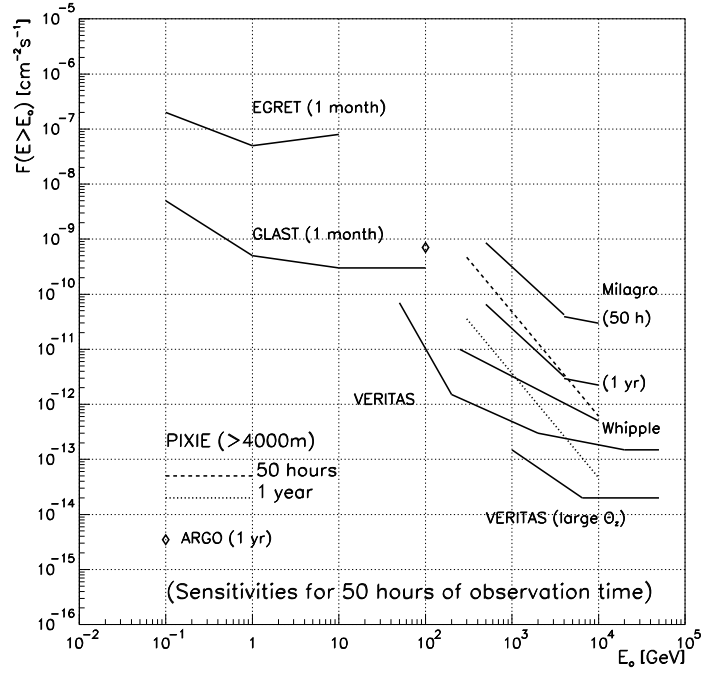


Fig. 11. Predicted sensitivity of some proposed and operational ground-based telescopes. The dashed and dotted lines show the predicted sensitivity of the telescope described here (PIXIE) at an altitude > 4000 m. The numbers are based on a 5σ detection for the given exposure on a single source. EGRET and GLAST sensitivities are for 1 month of all-sky survey. The ARGO sensitivity is taken from [25], all others from [30]. Information required to extrapolate the ARGO sensitivity to higher energies is not given in [25].

Acknowledgements

We thank the authors of CORSIKA for providing us with the simulation code; we also acknowledge D.G. Coyne, C.M. Hoffman, J.M. Ryan, and D.A. Williams for their useful comments. This research is supported in part by the U.S. Department of Energy Office of High Energy Physics, the U.S. Department of Energy Office of Nuclear Physics, the University of California (RSM), and the National Science Foundation (SW).

References

- [1] For recent reviews, see R.A. Ong, to be published in Physics Reports, and C. M. Hoffman, C. Sinnis, P. Fleury and M. Punch, to be published in Reviews of Modern Physics.

- [2] T.C. Weekes et al., *Astrophys. J.* 342 (1989) 379.
- [3] M. Punch et al., *Nature* 358 (1992) 477.
- [4] J. Quinn et al., *Astrophys. J.* 456 (1996) L83.
- [5] M. Catanese et al., *Astrophys. J.* 501 (1998) 616.
- [6] T. Kifune et al., *Astrophys. J.* 438 (1995) L91.
- [7] T. Yoshikoshi et al., *Astrophys. J.* 487 (1997) L65.
- [8] T. Tanimori et al., *Astrophys. J.* 497 (1998) L25.
- [9] C. Fichtel et al., *Astrophys. J. Suppl. Ser.* 94 (1994) 551.
- [10] D.J. Thomson et al., *Astrophys. J. Suppl. Ser.* 101 (1996) 259.
- [11] F. Aharonian et al., *Astron. Astrophys.* 327 (1997) L5.
- [12] E.D. Bloom, *Space Science Rev.* 75 (1996) 109.
- [13] D. Heck et al., CORSIKA: A Monte Carlo Code to Simulate Extensive Air Showers, Forschungszentrum Karlsruhe, Wissenschaftliche Berichte FZKA 6019 (1998).
- [14] S. Westerhoff et al., *Astroparticle Physics* 4 (1995) 119.
- [15] J. Matthews et al., *Astrophys. J.* 375 (1991) 202.
- [16] D.J. Fegan et al., in *Towards a Major Atmospheric Cherenkov Detector III*, ed. T. Kifune (Tokyo, Universal Academy Press, 1994) p.149.
- [17] P. de Barbaro and A. Bodek, University of Rochester Preprint No. 1389, University of Rochester (1994).
- [18] H.O. Klages et al., *Nucl. Phys. B (Proc. Suppl.)* 52B (1997) 92.
- [19] W.R. Nelson et al., SLAC Report 265 (1985).
- [20] K. Werner, *Physics Reports* 232 (1993) 87.
- [21] H. Fesefeldt, Report PITHA-85/02, RWTH Aachen (1985).
- [22] CERN Application Software Group, CERN W 5013, Version 3.21 (1994).
- [23] P. de Barbaro et al., *Nucl. Instr. Meth. A* 315 (1992) 317.
- [24] G.B. Yodh et al., *Space Science Rev.* 75 (1996) 199.
- [25] M. Abbrescia et al., ARGO proposal (1996), unpublished.
- [26] See for example G. Kaiser, *A Friendly Guide to Wavelets* (Birkhäuser, Boston, 1994).
- [27] R.S. Miller, in preparation.

- [28] A.M. Hillas et al., *Astrophys. J.* 503 (1998) 744.
- [29] K. Asakimori et al., *Astrophys. J.* 502 (1998) 278.
- [30] Proposal for the Gamma-Ray Large Area Space Telescope (GLAST), SLAC Report 522 (1998).

This figure "rmiller_fig4.jpg" is available in "jpg" format from:

<http://arxiv.org/ps/astro-ph/9812153v1>